Experimental Mechanics
https://doi.org/10.1007/s11340-021-00704-x

RESEARCH PAPER

Tribological Characterization of Gradient-density Polyacrylamide Hydrogel Surfaces

C. L. Johnson[1] · **A. C. Dunn**[1]

Received: 3 September 2020 / Accepted: 23 February 2021

Abstract

Background The contact and frictional response of a hydrogel is dependent on the polymer structure at the gel surface. Recent work has shown that different mold materials in contact with the gel during polymerization will affect the resulting polymer density.

Objective The tribological response of a gel with a 'brushy' less-dense polymer surface has not been thoroughly studied. Our goal was to perform a suite of tribological experiments to better understand the response of the less-dense layer.

Methods In this work, we conducted indentation, creep, and sliding experiments with various loads, speeds, and probe materials to determine the impact of the less-dense layer on the contact and frictional behavior of polyacrylamide hydrogels. We additionally used micro-fluorescent particle exclusion to measure the contact areas throughout each experiment.

Results Indentation revealed a non-Hertzian regime for the first 13–29 μm after first contact that has a weaker force response for a given indentation depth. Creep experiments showed that the surface layer relaxes poroelastically, with water exudation occurring within the gradient layer despite the low contact pressures. Friction was highly speed-dependent, with faster sliding speeds decreasing friction to values as low as 0.01; transient behavior was not seen for most of the experiments, suggesting that the surface layer is capable of quick water re-uptake when out of contact.

Conclusions We have provided a deeper understanding of the contact and frictional response of this gradient-density surface layer, which will prove useful for hydrogel designs requiring ultra-low friction in a dynamic application.

Keywords Polyacrylamide · Hydrogel · Indentation · Relaxation · Friction · Contact area

Introduction

The contact and slip mechanics of hydrogels are still relatively unknown. Despite this, there is a growing demand to engineer these materials for applications involving such scenarios. Current hydrogel research has a heavy focus on its use as a material for artificial tissues [1, 2]. Applications such as artificial cartilage are particularly suited for these hydrated gel networks due to their liquid-content similarity to cartilage. These gels can be up to 95% water, and experience optimal frictional and lubrication behavior approaching the conditions seen in a joint. Simple single-network gels are composed of a crosslinked structure of uniform mesh size, which creates a consistent, but brittle network. However, cartilage has a distinct composite-like heterogeneous structure that allows it to out-perform most hydrogels in lubricity and strength [3, 4]. It has thus far proven challenging to obtain both frictional and mechanical characteristics in a hydrogel approaching that of natural cartilage, since their structures are vastly different.

Attempts to design gels with favorable frictional and mechanical properties have used a myriad of approaches to change the gel's bulk structure. Many groups have opted for double-network hydrogels to improve modulus and toughness compared to a single-network gel [4–7]. However, the DN gel system tends to be chosen based on the properties of the individual networks without the possibility of iterative design. Others have used single-network gels with varying monomer/crosslinker concentrations in order to identify trends between composition

✉ A. C. Dunn
acd@illinois.edu

[1] Department of Mechanical Science & Engineering, University of Illinois at Urbana-Champaign, Urbana, IL 61801, USA

Published online: 15 March 2021

and lubricity. But previous work investigating friction based on composition has revealed complex, and seemingly contradictory, behavior. Polyacrylamide (pAam) hydrogels have shown a friction minimum at 6% acrylamide concentration, but differing speed dependence for different monomer concentrations [8]. Li et al. found that polyacrylamide gels experienced higher friction for larger monomer concentrations and decreased friction as the degree of crosslinking increased [9]. A study using an alginate/polyacrylamide IPN gel found higher friction for a larger crosslinker concentration at sliding speeds below 50 mm/s [10]. However, work with PVA gels found higher friction for more densely crosslinked gels [11].

An explanation for these conflicting results comes from recent work by Meier et al., who found that the local surface structure of a hydrogel depends on the material it was molded against. They discovered that polyacrylamide gels molded against different counterface materials produced gels with different indentation-derived moduli, suggesting the hydrophobicity of the mold surface as the defining factor [12]. Glass surfaces resulted in larger moduli, while polymer surfaces created more compliant gels. Their work suggests a non-uniform gel structure, with decreasing polymer/crosslink density at the surface compared to the bulk that is responsible for additional compliance and lubricity. Further work by Gombert et al. confirmed the existence of this 'brushy' surface layer in a polystyrene-molded hydrogel using neutron reflectometry and infrared spectrometry [13].

This information suggests that the contact/frictional response of a hydrogel is almost entirely controlled by the local chemical and physical structure at its surface. However, the nature of this surface layer has not been characterized in depth. Proper study of the surface layer's structure and contact response is a necessary step towards design of better tissue surrogates. Such knowledge would provide a way to engineer composite, structurally heterogeneous hydrogels with favorable frictional and mechanical properties solely through intentional mold material selection.

In this work, we created 7.5% pAam hydrogels molded against polystyrene surfaces and assessed their surface properties through micro-indentation, creep, and sliding experiments. By analyzing measurements of normal/friction force, indenter depth, and contact area, we show that the 'brushy' low-density gradient layer at the surface of the hydrogel controls its contact behavior and lubricity. The layer experiences poroelastic relaxation under applied pressure but can quickly recapture ambient water to maintain lubricious conditions during sliding. This gradient layer provides another method to design for an ultra-low friction hydrogel independent of the chemical composition.

Methods

Materials

Polyacryalmide hydrogels were created using stock solutions of acrylamide (Aam) monomer, methylenebisacrylamide (BisAam) crosslinker, tetramethylethylenediamine (TEMED), and ammonium persulfate (APS). These solutions were combined to create a pre-polymerized solution of 7.5% wt/wt Aam, 0.3% wt/wt BisAam, 0.15% wt/wt TEMED, and 0.15% wt/wt APS. This solution was quickly poured into cylindrical polystyrene molds of diameter 35 mm and height 4 mm, then covered with a polystyrene surface in contact with the solution. After allowing the gels to cure in the mold for one hour, the gels were cut down to a 25 mm diameter and placed in a DI water bath for at least 24 h prior to testing.

Polyacrylamide hydrogel probes of identical composition were polymerized onto an aluminum stud using a custom-made mold of Delrin and poly-olefin plastic parts. After 30 min, the probe was removed from the mold and hydrated in DI water for at least 24 h.

Overview

All experiments used an experimental setup consisting of a microtribometer mounted atop a confocal microscope [14]. Two contact types were tested: a rigid spherical probe indenting into a flat hydrogel surface ('soft-substrate' or 'migrating' during sliding), and a hydrogel hemispherical probe indenting into a flat hydrogel slab ('Gemini' contact) (see Fig. 1). The hydrogel probe for Gemini contact was molded onto an aluminum stud using a poly-olefin mold. Probes had a diameter of 4 mm. The flat hydrogel substrates were cylindrical with a 25 mm diameter and 4 mm thickness.

The indenting force was applied through precise vertical movement of a four-bar cantilever. Capacitive sensors placed 25 μm from the tribometer flexure allowed normal and lateral force measurements throughout each experiment at a rate of 100 Hz (see Dunn et al. for more information [14]).

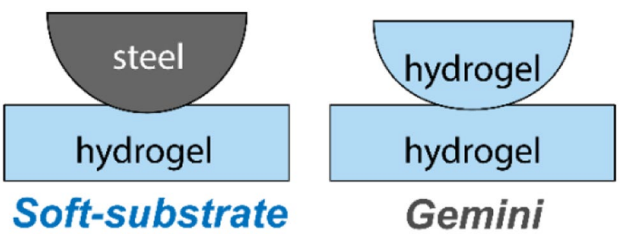

Fig. 1 The two contact setups used for all experiments. Soft-substrate (left) contact uses a rigid spherical probe. Gemini (right) contact uses a hydrogel probe molded onto a stud

A dilute solution of 0.5 µm green fluorescent particles in de-ionized water was poured on top of the flat hydrogel. Light of wavelength 470 nm was passed through a filter up towards the bottom of the sample to induce light emission in the particles and observe their movement via the confocal microscope. As the indenting probe approached the counterface, the fluorescent beads cleared the emerging contact due to fluid pressure, forming a distinct region devoid of particles that corresponded to the nominal contact area (see Fig. 2). Video of this contact area projection was captured for each experiment at 15 fps using the confocal microscope and its accompanying program (Nikon Analysis) (see online supplemental material section for video examples).

Indentation Experiments

Short-duration, displacement-controlled indentation was performed. Indent and pull-off each occurred over a 5 s linear ramp; dwell time was kept to zero. Maximum stage depth was set by recording the vertical displacement corresponding to a nominal load of approximately 500, 750, or 1000µN, and then indenting to this depth for the actual experiment. Normal force and stage displacement were acquired at a rate of 100 Hz. Experiments were performed on areas of the gel at least 4 mm away from each other, with ten minutes in between indentations to allow the gel to fully re-equilibrate (Table 1).

The contact area videos were anchored together with the indentation data by matching the time of maximum indent depth to the time of maximum contact area. Video snapshots were extracted at 0.5 s intervals and analyzed for contact area. Nominal pressures were calculated using the

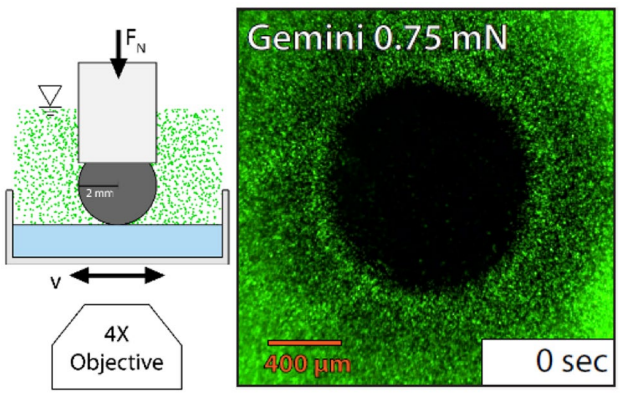

Fig. 2 'Exclusion' technique used to determine contact areas in-situ during all of the experiments (left). The microfluorescent particles clear the contact, leaving a zone devoid of particles corresponding to the contacting area (right). All contact was submerged under water. Soft-substrate contact is shown. Gemini contact instead used a hydrogel probe. For sliding experiments, the hydrogel, attached to a reciprocating stage, was translated at a constant velocity. Components not to scale

Table 1 Loading rates of each indentation experiment

Indentation Experiment (Max Load)	Loading Rate [µm/s]
Soft-substrate (500µN)	19.2
Soft-substrate (750µN)	18.2
Soft-substrate (1000µN)	20.8
Gemini (500µN)	21.3
Gemini (750µN)	26.1
Gemini (1000µN)	32.9

accompanying normal force at that particular time. The time of first contact in each video was recorded.

The indentation portions of each experiment were analyzed using a force-derivative method developed by Garcia et al. [15]. In the first step of the method, a derivative of the force eliminates the need to know the contact point so that a single-parameter fit can be done for the modulus of elasticity; in the second step, another single-parameter fit locates the point of contact. The method takes advantage of the power law form of contact models, and especially the relation between force and indentation depth. This allows the derivative of the force with respect to depth, dF/du, to be expressed as a power of the force itself, F^n, times a constant, K_G (equation (1)). A straight line on the log–log plot of dF/du versus F corresponds to a line of slope n with intercept log(K_G).

$$\frac{dF}{du} = K_G F^n \tag{1}$$

In equation (1), $K_G = PK^{1/P}$ and $n = (P\text{-}1)/P$. K is a coefficient containing the constants associated with the force–displacement relationship of a particular contact model, such as reduced modulus, indenter radius, etc. P is the exponent relationship between the force and displacement for the contact model. For example, Hertzian contact has $P = 3/2$ and $n = 1/3$. The reduced modulus is found from fitting a power-law model to the data using least-squares error minimization to determine the value of K_G. This leaves the point of contact as the only unknown, allowing the force-depth curves to be curve fit to a Hertz model using MATLAB's least-squares algorithm. This gives d_{Hertz}, the Hertz-predicted point of first contact. By using this method by Garcia et al., a two-parameter fit with multiple possible "optimal" solutions can be split into separate single-parameter fitting steps to truly minimize error.

Creep Experiments

Long-duration force-controlled experiments were conducted to view contact area expansion over time. A fixed normal load of 500, 625, 750, 875, or 1,000µN was applied by the

probe onto the gel substrate for at least 600 s. This load was servo-ed in real time every 0.1 s, allowing the tribometer vertical stage to adjust to maintain the prescribed load (within = ±20μN).

Snapshots from the microscope video output were taken at 30 s intervals up to 180 s and 60 s intervals thereafter. Image sizes were 512×512 pixels, corresponding to real dimensions of 2.05×2.05 mm. Contact areas were measured using ImageJ's convex hull fitting algorithm and built-in area calculation. Standard deviation of the contact areas was determined by taking a representative image for a particular experiment and repeating the area calculation ten times. Average contact pressures were calculated at each of these intervals by dividing the prescribed force by the nominal contact area. Standard deviation of pressure was calculated using error propagation and the uncertainties of the force and area.

Sliding Experiments and Data Analysis

A linear reciprocating stage with stroke length 1,500 μm was used to move the sample relative to the fixed probe. Experiments were conducted at 1,000μN and three stage speeds (10, 30, 100 μm/s). The prescribed load was maintained through computer-controlled adjustments of the vertical stage at the beginning of each cycle. Experiments lasted at least 600 s, corresponding to at least 2, 6, or 20 cycles for each of the respective aforementioned speeds.

Contact area was analyzed using an image stack averaging method to more clearly determine the contact boundaries. Each stroke length was divided up into six equal sections composed of at least 200 video frames each. The frames of each section had their color intensities averaged, creating six composite images spread across the stroke length. Image subtraction between two adjacent composite images revealed differences in particle locations over that elapsed time span, such as particle flow patterns and contact boundary shifts. This allowed clear demarcation of the contact boundaries.

Results

Indentation Experiments

Indentation experiments showed a Hertz-like response at the data points clearly past the point of contact (Figs. 3, 4). The Garcia method was used to fit the data points to the Hertz model, which on a plot of dF/du vs F is represented by a power law relationship with $n = 0.33$. The reduced modulus was calculated from the K coefficient

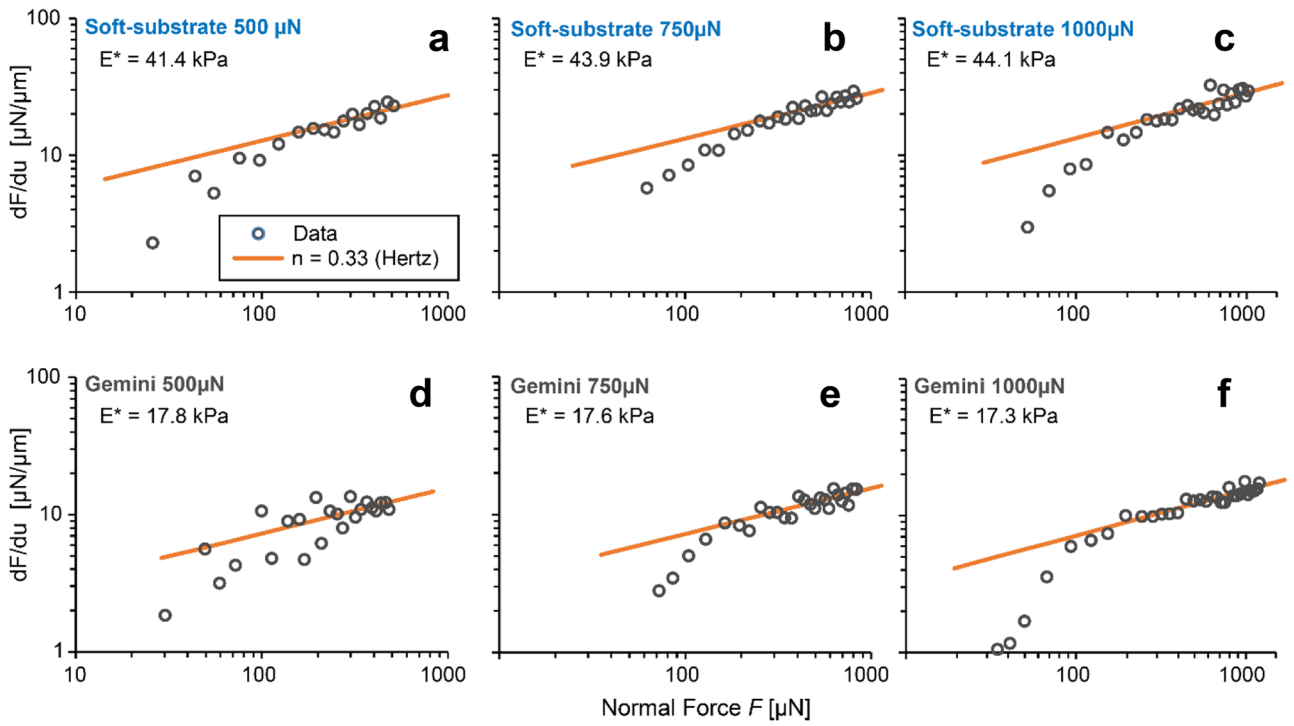

Fig. 3 The Garcia method of modulus determination showed that the higher force points, and thus higher displacement points, fit well to a Hertz contact model ($n = 0.33$). Extracted moduli were 41.4–44.1 kPa for soft-substrate contact (**a-c**) and 17.3 – 17.8 kPa for Gemini contact (**d-f**). Low force portions of the indentation data deviated from the Hertz model. Data points are the average of 10-point bin averaging

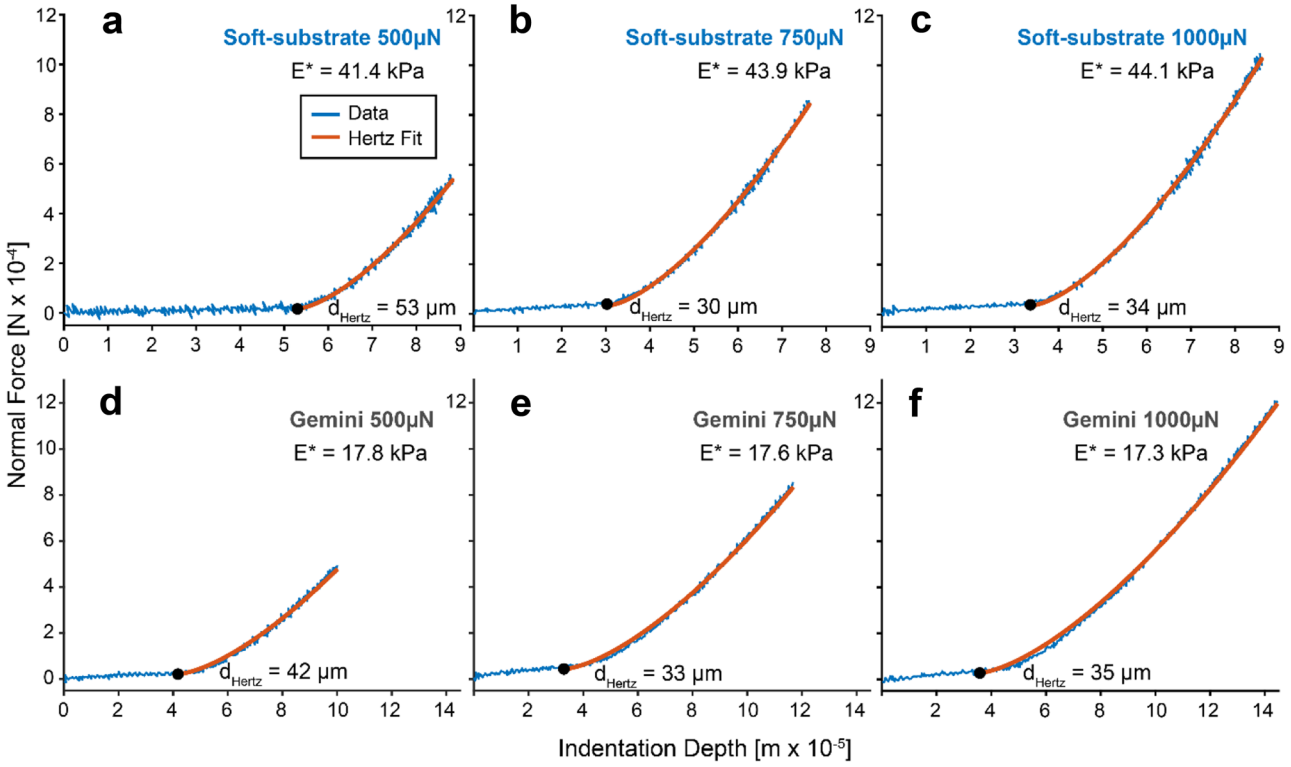

Fig. 4 Soft-substrate (**a-c**) and Gemini (**d-f**) force-indentation depth curves with Hertz fits using the force derivative method [15]. The predicted point of contact, d_{Hertz}, was found by least-squares curve fitting

that emerged from the single-parameter fitting. For soft substrate, it ranged from 41.4 to 44.1 kPa; for Gemini it was a range of 17.3–17.8 kPa. In each measurement there are points which disobey the Hertz contact theory because they do not fit well to $n = 0.33$.

Contact modeling is typically plotted as force-depth curves in which the forces and indentation depths have been drawn back to some point of contact. Because we have already fit the curves for the reduced modulus above, a second fitting step of the force-depth curves can be used to find the predicted point of contact: the depth at which first contact occurs according to the Hertz contact model, d_{Hertz} (Fig. 4). Here, the magnitudes of d_{Hertz} represent the stage position between the start of the vertical motion and the theoretical point of contact. It should be noted that, though careful measures were taken to fit the data, this contact point is not yet confirmed, and is only the product of fitting a function. The points in the low-force regime which disobey the Hertz model are obscured because of the linear scales, and as such we confirm further support for methods like Garcia et al. propose [15], which do not rely on 2-parameter fitting without a sensitivity analysis for each parameter.

Traditional force-based contact mechanics would rely on the above analysis to provide insight into the contacts. However, we simultaneously recorded videos in situ using fluorescence microscopy to identify the time of first contact and real areas of contact. Anchoring the microscopy with the force data provided the indentation depth of true first contact, $d_{contact}$. In a perfect Hertz contact situation, the real stage position at time of contact would coincide with the indentation depth of zero predicted by the Hertz model. While $d_{contact}$ and d_{Hertz} are within a few microns, the Hertz model fit of Fig. 4 is poorest near d_{Hertz}, which is located within the low-force, non-Hertzian regime of Fig. 3. Revisiting the technique of Fig. 3, we now fit the low-force data using equation (1) for an exponent n which minimizes error for all 3 measurements of each configuration; the coefficient K_G was re-solved for each attempted fit to minimize error for a given n. For soft-substrate contact, an average exponent of $n = 0.7$ best fit this data (Fig. 5(a-c)), while Gemini contact fit to an exponent $n = 1.5$ (Fig. 5(d-f)).

In order to quantify the difference between actual contact and the model-predicted contact, we identify the closest data point to the intersection of these model fits as d_{match} (Fig. 5). Further, we define Δd as the difference between $d_{contact}$ and d_{match}; the magnitude of Δd can be considered a penetration depth before the Hertz contact model applies. The value of Δd was consistently around 16 μm for soft-substrate contact. Gemini contact had a wider range of Δd

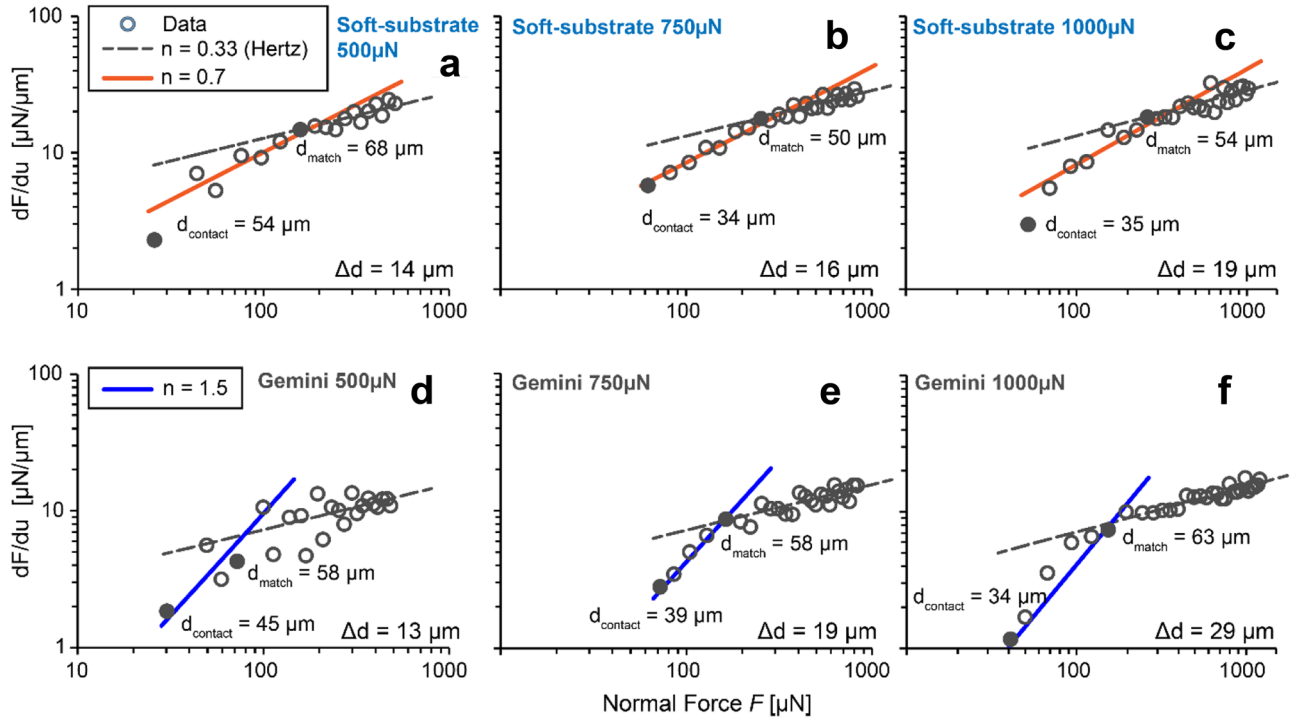

Fig. 5 Force derivative dF/du vs F plots of the indentation data, a fitted Hertz model, and a model with $n=0.7$, 1.5. Data points only after first contact are plotted. Δd is the difference in indentation depth between the video-determined point of contact, $d_{contact}$, and the point where both fitted models converge, d_{match}, both shown with filled data points. It provides a measure of the necessary compression of the less-dense layer before emulating the response of the bulk. Data points are the average of 10-point bin averaging

values reaching as high as 29 μm. Thus these plots indicate a soft region at the outer surface that the indenter must push through before a Hertz contact applies. However, for at least the first 13–29 μm, the influence of this layer was significant in the force response.

In addition to the force-depth information, it is generally agreed that for a stiff probe indenting a soft substrate, the contact radius a grows with the square root of indentation depth d according to the geometry of a spherical cap. The simultaneous measurement of depth and contact area can be used to assess how well these real contacts obey this compatibility equation. A plot of the normalized contact radius versus the normalized indentation depth is expected to obey the relation $a = R^i d^j$, where $i=j=0.5$

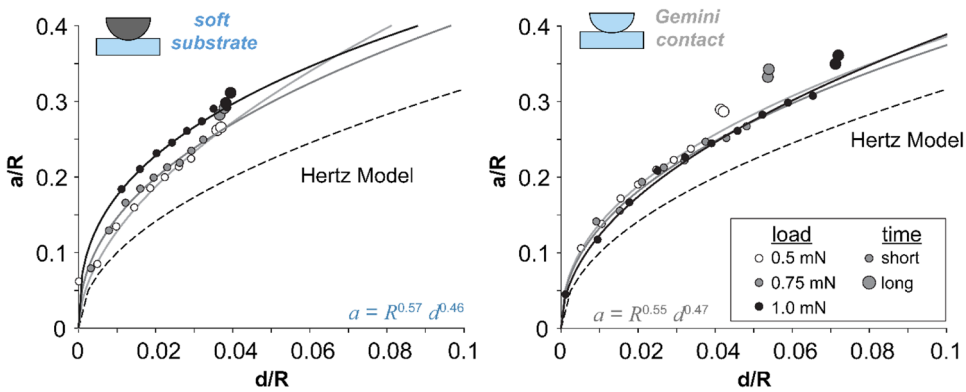

Fig. 6 Fits for the compatibility equation relating contact radius to indentation depth show a deviation from Hertz contact; contact radius was consistently under-predicted. In both contact setups, the contact radius depends more on the probe radius than the indentation depth (compared to Hertzian contact compatibility). Creep experiments ('long' time points) matched the compatibility equations for soft-substrate setups (left)

(Fig. 6 Hertz model). For all indentations performed, a Hertz fit under-predicted the contact area during indentation. Fits of a compatibility equation of the form $a = R^i d^j$ showed that the contact area had a stronger dependence on the probe radius (soft substrate i = 0.57 and Gemini i = 0.55), and weaker dependence on the indentation depth (soft substrate j = 0.46, Gemini j = 0.47). The contact radii of the soft-substrate experiments were underpredicted to a greater extent than the Gemini tests. Each fitted curve from the soft-substrate experiments had greater deviation for larger maximum loads. This shows a strong loading-rate dependence for this contact type. In contrast, Gemini contact showed no loading-rate dependence.

Creep Experiments

Creep experiments confirmed an increase in the contact area with time (Fig. 7). The majority of contact area gain occurred within the first 100 s regardless of contact setup. Contact area growth from the initial contact area was highest for the lowest applied loads, with a 40% increase. Higher loads experienced less area growth relative to the initial area, only rising ~ 30% over the full 600 s experiment. The average contact pressure in these experiments remained low. Initial pressures ranged from 0.5 to 1.4 kPa and decreased up to 40% due to contact area growth.

Sliding Experiments-Pressure vs Time

The creep of the contact areas under an indenting probe was demonstrated in Sect. 3.2, where increasing contact area corresponded to decreasing contact pressure because the load was held constant. The contact area evolution in sliding conditions did not follow the indentation behavior. Instead, the contact area decreased slightly, which increased pressure. Contact area dropped by 15–24% at the onset of sliding, remaining near this new value for the duration of the experiment (Fig. 8).

Further, the pressure was relatively constant after a brief run-in period. For soft substrate i.e. migrating contact, a steady-state sliding pressure of 1.12 to 1.15 kPa was reached for all sliding speeds within the first 100 s (Fig. 9). This corresponded to a 20% pressure increase over the initial contact area prior to sliding. The steady-state pressure was reached faster for quicker sliding speeds: 60 s for a 30 µm/s sliding speed and 18 s for 100 µm/s sliding speed. However, all three experiments reached steady-state pressure shortly after a single stroke length of total sliding distance. The steady-state contact area was nearly the same across the three tested speeds, which implies that steady-state contact area and contact pressure are either insensitive or independent of the sliding speed.

Gemini contact showed a similar 15–20% pressure increase over the non-moving case. The pressure remained at a value of 0.78 kPa regardless of sliding speed due to the constant contact area during sliding.

Sliding Experiments-Friction vs Time

Friction of soft materials is typically related to contact area, and serves as a metric indicating the amount of energy needed to maintain slip. For the migrating contact case, friction remained constant or even decreased

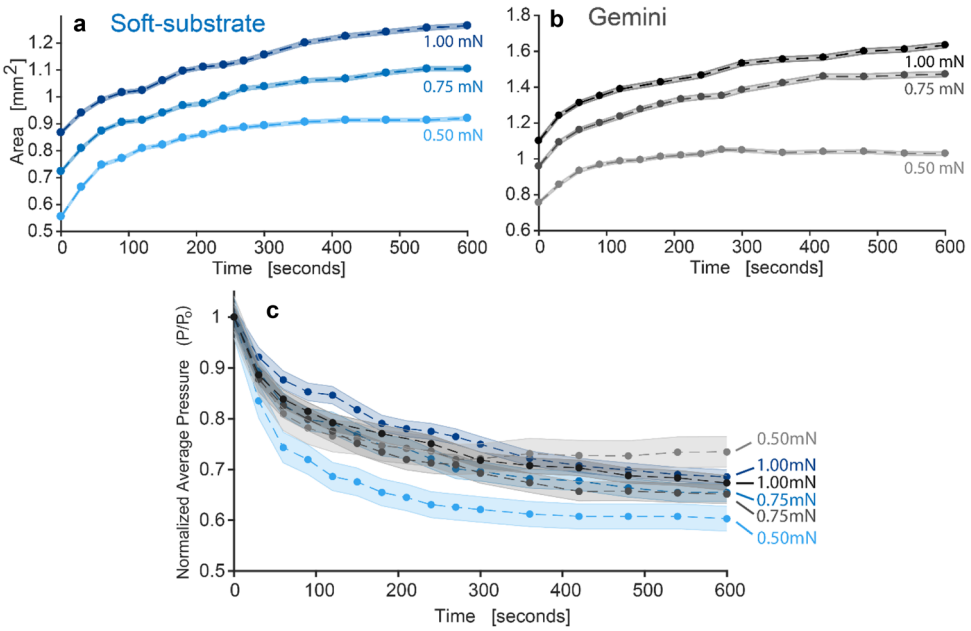

Fig. 7 Area increased over time for both soft-substrate (**a**) and Gemini (**b**) contact setups. Contact areas increased most rapidly for the first 100 s after first contact. Contact area uncertainties were calculated using a representative image of each experiment and repeating the contact selection 10 times. Normalized pressure (**c**) decreased to a similar magnitude of roughly 70% of the original pressure for all experiments. Error was evaluated using propagation of uncertainty.

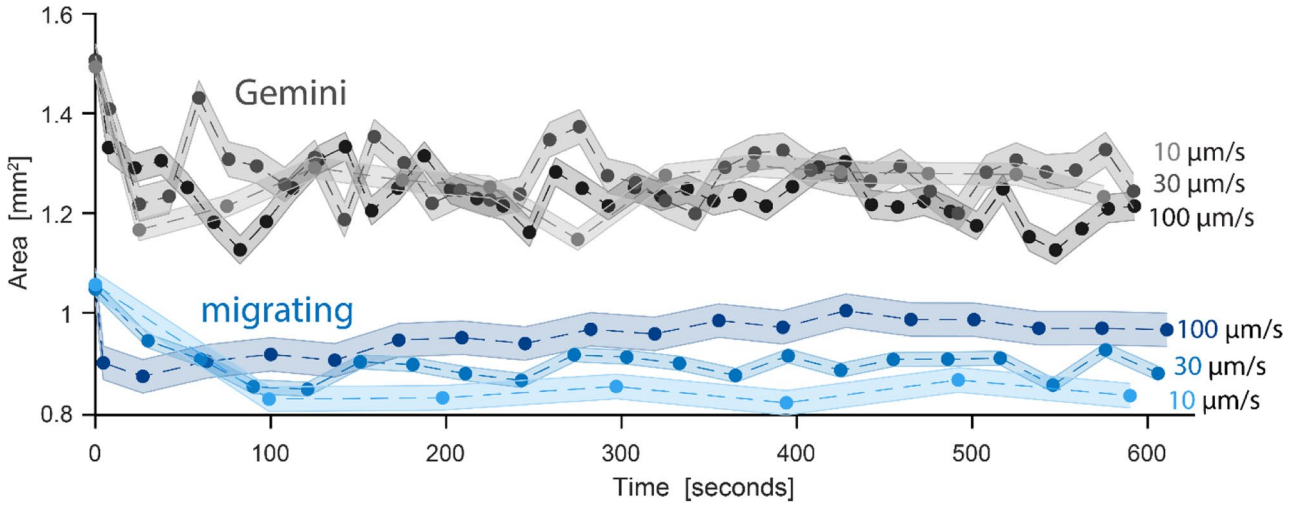

Fig. 8 Contact area vs time for the sliding experiments. Any degree of movement resulted in a contact area decrease compared to the non-moving case of ~ 20%. Normal load was 1000 µN. Uncertainty was determined by repeating an area calculation on a representative image of the experiment ten times, then taking the standard deviation

with time, with sliding speed inversely correlated to friction coefficient (Figs. 10, 11). After the first full pass, the coefficient of friction stabilized at $\mu = 0.026$ for a 100 µm/s sliding speed and 0.039 for a 30 µm/s sliding speed. For the slowest sliding speed of 10 µm/s, friction coefficient dropped from 0.097 to a steady-state value of 0.085 after the first cycle. The steady-state friction coefficient at 10 µm/s was over three times the magnitude as the coefficient at 100 µm/s. Friction at 30 µm/s was 50% larger than at 100 µm/s.

For Gemini contact, friction coefficient was steady at $\mu \approx 0.01$ at a 100 µm/s speed, which matches well with experiments conducted at higher pressures of 6 kPa by Gombert et al. [13]. Friction increased over time for the 10 µm/s sliding speed, starting from 0.025 and doubling to 0.05 over the course of 600 s. This transient behavior was exclusive to the slowest sliding speed; the 30 µm/s

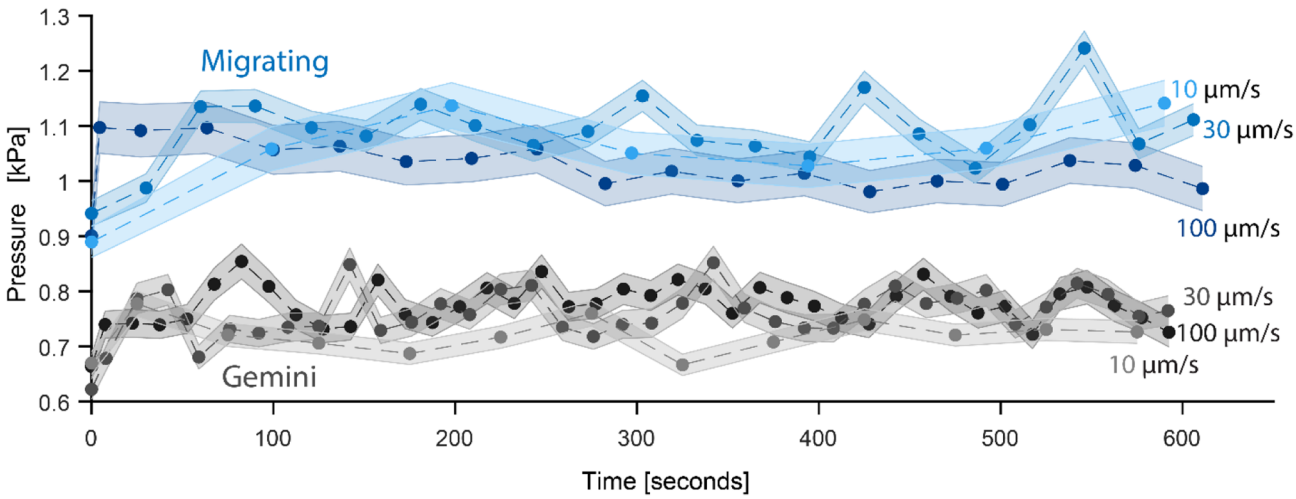

Fig. 9 Contact pressure decay was suppressed by any degree of sliding. Pressures increased by 20% compared to the non-moving case, with slower speeds taking longer to reach this steady-state pressure value. Sliding speed did not influence the magnitude of this final pressure. For all sliding speeds, migrating contact pressure stabilized around 1.15 kPa, while Gemini contact experienced a pressure of 0.76 kPa. Normal force was 1,000 µN. Uncertainties of each point were calculated using uncertainty propagation of the force and contact area standard deviations

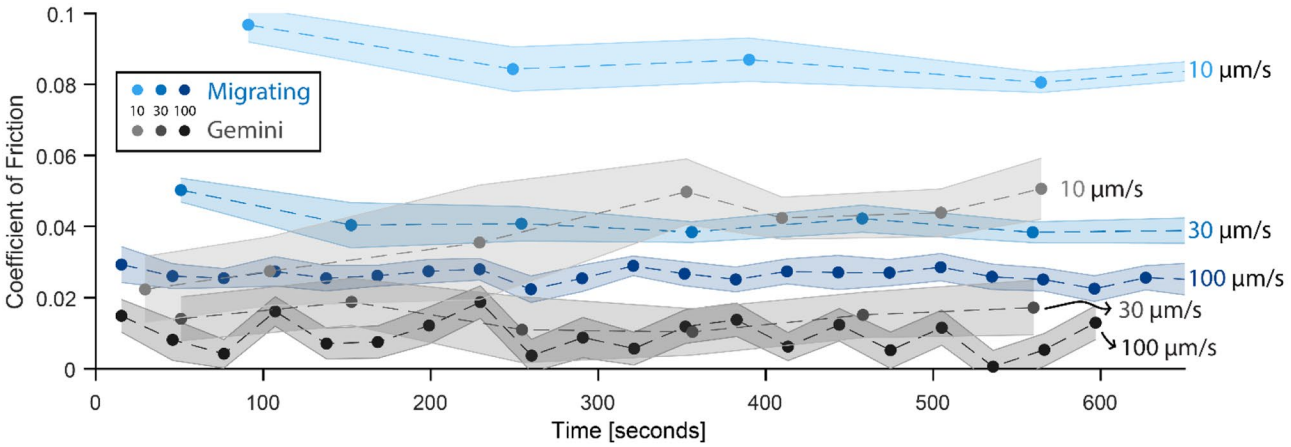

Fig. 10 Friction coefficient quickly stabilized for migrating contact and faster Gemini sliding, but was transient for Gemini contact moving at 10 µm/s. For migrating contact, it stabilized after the first complete cycle regardless of sliding speed. Gemini contact at 10 µm/s sliding speed saw an increase in friction over the course of the test. Gemini contact appeared to exhibit a set minimum friction coefficient of 0.01 as speed increased. Migrating contact friction was at least twice as large as in a comparable Gemini contact experiment. Normal force was 1000 µN. Friction coefficient was calculated as an average value over each complete reciprocating cycle. Uncertainty bounds correspond to the standard deviation of the friction coefficient throughout the cycle

and 100 µm/s sliding speeds had constant friction coefficients of 0.015 and 0.011 respectively.

Discussion

The suite of contact and sliding experiments presented in this work allows for a comprehensive argument in support of the inherent existence of a soft surface layer at the boundary of high-water-content polyacrylamide hydrogels molded against polystyrene countersurfaces. Here we discuss the findings in detail toward this end.

Contact Mechanics

The presence of a gradient polymer density layer causes indentation behavior to differ from expected contact models. Our experiments show that a polystyrene-molded hydrogel surface experiences a distinctly non-Hertzian response

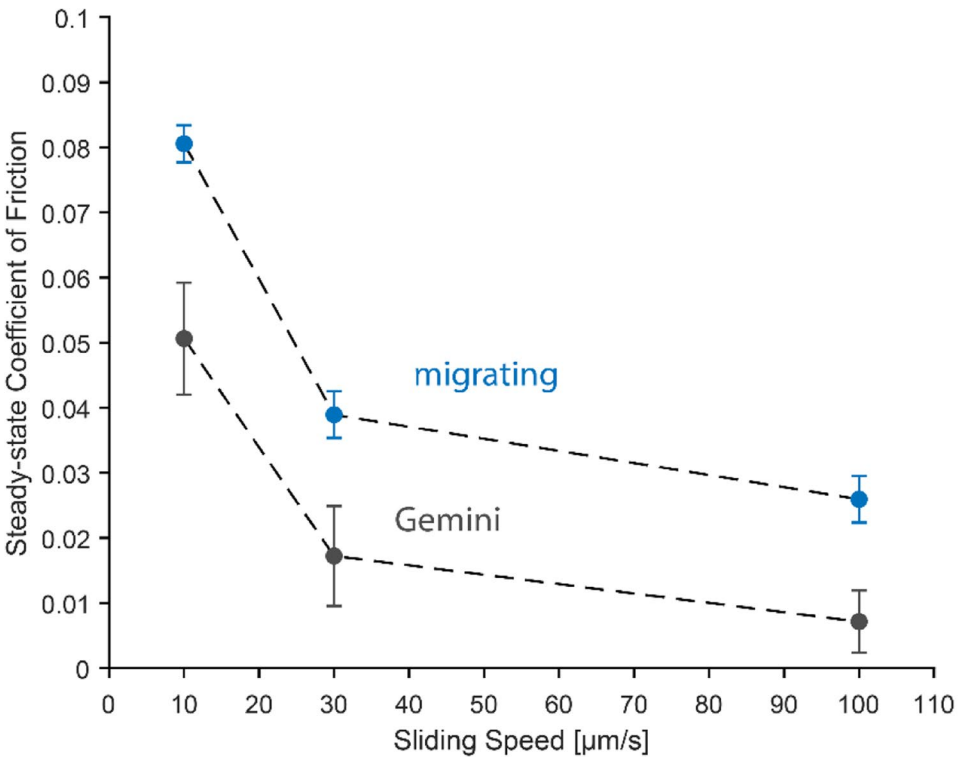

Fig. 11 Steady-state friction coefficient decreased with increasing sliding speed for both contact configurations. Gemini contact exhibited friction coefficients less than half that of migrating contact. Friction coefficients, and their respective errors, were determined using the average coefficient over the last 150 s of each experiment

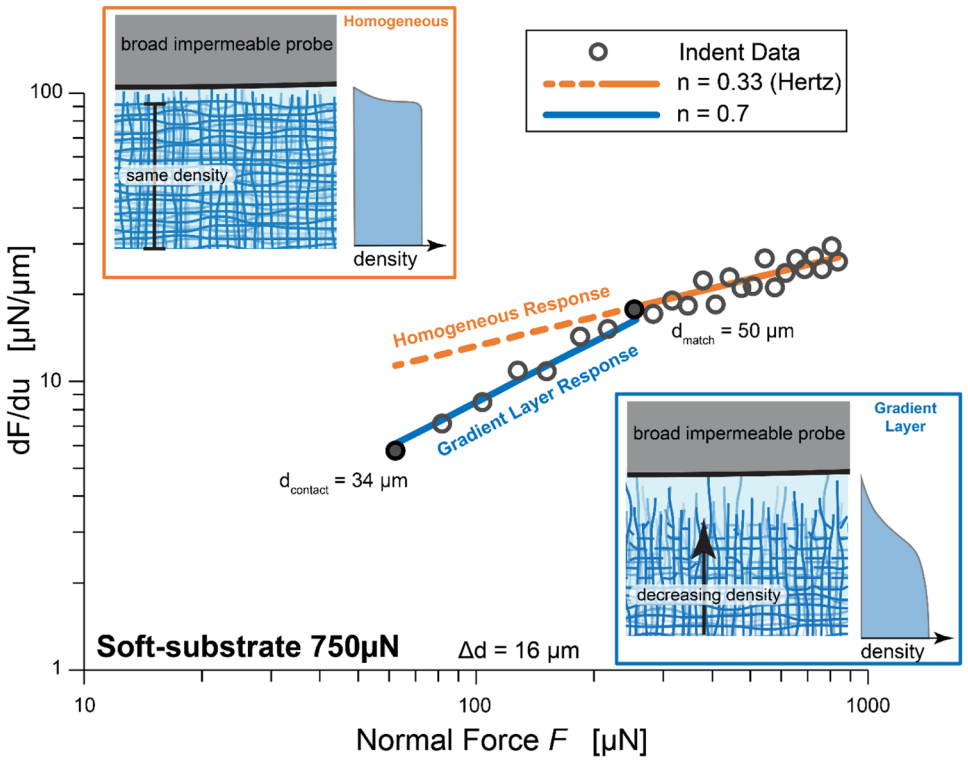

Fig. 12 Log–log plot of dF/du vs F for one soft-substrate indentation experiment (Fig. 5**b**). The blue fit line gives the fitted behavior before Hertz behavior holds true (orange solid line). In a more homogeneous 'neat' hydrogel, such as one molded against glass, the expected response would be Hertzian (orange dotted line)

for the initial 13–29 μm of indentation (Fig. 12 blue line). This differs from previous studies that have shown synthetic glass-molded hydrogels to exactly follow Hertzian contact throughout miscroscale indentation [16, 17]. Our polystyrene-molded gels required an indentation penetration of, on average, 16 μm beyond initial contact before a Hertz model adequately fit the data (see Figs. 5, 12). This Δd offset can be considered the compression of the less-dense layer required in order to emulate the response of the bulk. Simic et al. suggested that the thickness of the 'brushy' layer was on the order of 10–20 μm [18], and our Δd values confirm this order of magnitude.

It is challenging to describe the soft layer contact mechanics using an existing model. Fitting a model with the form of equation (1) to the non-Hertz portion of the indents resulted in $n = 0.7, 1.5$. The exponent n is related to the force power-law sensitivity for a given indentation depth u as: $F^{(1-n)} \sim u$ (integration of equation (1)). For Hertz contact, this becomes the well-known relation $F^{2/3} \sim u$. The soft-region fitting for soft-substrate and Gemini contact gives $F^{0.3} \sim u$ and $F^{-1/2} \sim u$, respectively, equivalent to $F \sim u^{3.33}$ and $F \sim u^{-2}$. The former implies a stronger force response compared to Hertz or Winkler contact. The latter, being a negative coefficient, suggests that the force decreases during indentation into the soft layer. Within the first few microns of indentation, contact would approximate that of a polymer brush approaching a rigid counterface or a similar polymer brush (Gemini). In the first case, corresponding to soft-substrate contact, analytic modeling of an AFM probe indenting deeply into a polymer brush predicts a force-depth relationship of $F \sim u^3$, corresponding to an n exponent of 0.67 [19]. For Gemini contact, there is little background for sparse self-mated polymer brush contact in a hydrated environment. The character and extent of their interaction is suggested as a topic for further study. In physical contact models, the exponent n should be above zero. Fluid mechanical effects may be responsible for outlying n values.

Contact Area Creep

Time-dependent behavior can arise from various mechanisms. Here we consider viscoelasticity and poroelasticity, the mechanics which may describe the contact area creep observed in our porous crosslinked hydrogels. Viscoelasticity in contact mechanics is a bulk property, and as such should exhibit a common time constant for a given composition that is independent of the applied load [16, 20]. In contrast, poroelastic time constants are dependent upon the pressure driving the fluid; in this case the pressure is higher under larger applied loads. In the present work, a single characteristic time constant τ was determined for each creep curve by fitting a simple exponential function (Fig. 13). The time constants ranged between 100–300 s for the soft substrate setup, and 40–270 s for the Gemini contact. These ranges suggest that these contacts are not representative of a homogeneous viscoelastic material. This is in agreement with previous microscale experiments with polyacrylamide gels,

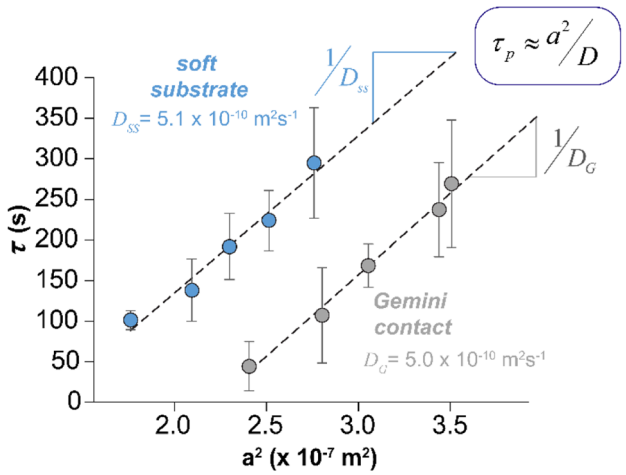

Fig. 13 A steady-state poroelastic diffusion coefficient calculated for both contact types results in similar values on the same order of magnitude as seen previously for polyacrylamide hydrogels. Uncertainty of the time constant was determined using error propagation of the contact areas used in the exponential model

which have shown a low degree of viscoelastic relaxation compared to poroelastic relaxation [21].

Poroelastic theory suggests that a single diffusion coefficient D relates the observed contact area and a single characteristic time constant fit to an exponential of the creep curve [22]. Best-fit lines of the points from each contact type indicate steady-state diffusion, as both were roughly 5×10^{-10} m^{2}s^{-1}, which is similar to values for hydrogels used to demonstrate poroelastic theory.

The time and diffusion constants extracted from migrating and Gemini creep experiments suggests poroelasticity as the primary relaxation method. However, poroelastic relaxation requires fluid squeeze-out from the pores. Since it is the osmotic pressure that retains the water in the polymeric mesh, poroelastic relaxation requires the applied pressure to exceed this pressure. The osmotic pressure of a hydrogel is dependent on its mesh (pore) size, which is linked to the distance between crosslinks [23]. For example, Schulze et al. determined an osmotic pressure of 11 kPa to induce water squeeze-out in 7.5% polyacrylamide gels molded against glass substrates, which had a predicted mesh size of 7 nm [24].

But the structure of a hydrogel surface is dependent not only on composition, but also on the mold material in contact with the gel during polymerization. Indentation experiments by Meier et al. have shown that glass mold substrates produce gels with larger moduli than those molded against polymer surfaces [12]. Further work by Gombert and Simic utilized infrared spectroscopy to show that there is a reduction in crosslink density near the surface of polymer-molded gels that produces a 'brushy,' less-dense structure, while a glass-molded gel surface is 'neat' with similar crosslink density as the bulk (see Figs. 12, 14) [13, 18]. This difference is predicted to come about due to the surface tension of the mold substrate and the interface strength of the polymerization solvent [25].

A structural and physical gradient at the surface would alter the osmotic pressure and elastic properties. Such physical gradient would decrease the osmotic pressures to zero at the boundary with the open bath, leading to local water readily exuding out at *any* applied pressure. Because the hydrogels in this work were molded against polystyrene, we can assume that our resulting 'brushy' gels experienced localized poroelastic relaxation of the less-crosslinked structure near the surface. Though our nominal pressures were at most 10% of the osmotic pressure, the permeability of the gel goes to infinity at the boundary, suggesting that poroelastic relaxation would occur within the layer at any pressure. However, a greater portion of the less-dense layer would experience water exudation for higher pressures, leading to a gradient poroelastic effect.

Sliding

The less-structured layer at the surface causes these gels to exhibit sliding characteristics resembling those of ultra-soft hydrogels. We observed asymmetric contact areas for migrating sliding, with the trailing edge of contact having a larger radius of curvature that was offset towards the leading edge (Fig. 15). This sliding

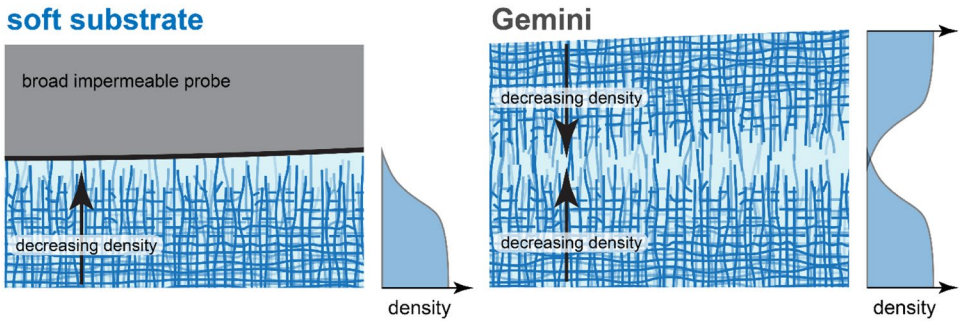

Fig. 14 Based on the polymer density reduction at the surface found by Gombert/Simic [13], we propose that a density gradient exists where the polymer/crosslink density is uniform in the bulk, but approaches zero towards the surface. Such a structure would change the local pore size, allowing water squeeze-out to occur sooner than in the bulk

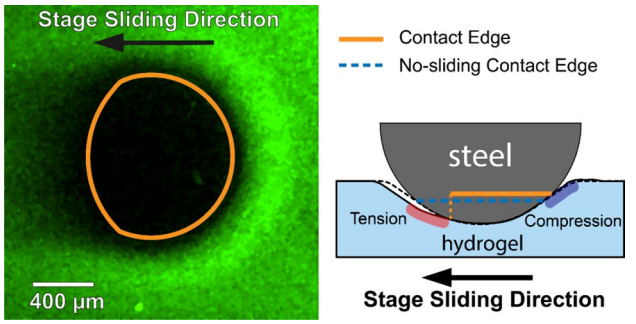

Fig. 15 Asymmetric contact areas were observed for all migrating contact sliding tests. These are likely due to compressive and tensile zones at the leading and trailing edges of the contact, respectively

contact asymmetry has only been observed for glass-molded polyacrylamide gels of much lower monomer percent (< 3.75% Aam) [26], providing further support for the existence of a less-dense surface layer for our gels. McGhee et al. suggests that this asymmetry is a result of the viscoelasticity of the high water content gel, which may have a greater influence on elastic behavior within the gradient layer of our gels. The compliance of the top layer leads to a compressive zone at the leading edge of the contact and a tensile zone in the wake of the contact.

In soft hydrogels, sustained pressure on the network will induce water squeeze-out, causing higher friction over time. But despite our gels showing signs of poroelastic relaxation within the less-dense layer, they exhibited consistent friction coefficients throughout each experiment. For migrating contact, the time to reach steady-state pressure was far shorter than the time to reach steady-state friction. The time of the former was roughly 60% of the latter for the 30 and 100 μm/s sliding speeds, and 20% for the 10 μm/s speed. This may occur due to re-orientation of the loosely crosslinked surface chains during the first few passes, providing less resistance to sliding for future cycles. Such behavior emulates floculation in complex fluids, and has been modeled by Kim et al. to describe the torque response of 'brushy' 7.5% pAam hydrogels [27]. Slower speeds may provide more time for chains to interact with the probe, resulting in a larger friction coefficient as the 'bonds' between the chains and probe are broken.

However, transient behavior was observed for one Gemini experiment sliding at 10 μm/s. The increase in friction may be due to pore squeeze-out under the probe made possible by the slow sliding speed. Reale et al. found that startup friction increases with longer indentation dwell time due to dehydration of the contact patch [28]. This water exudation leads to increased friction due to adhesion, which has been observed in indentation adhesion experiments conducted by Lai et al. [29]. For the 10 μm/s experiment, a typical contact diameter during sliding was 1,250 μm. Each portion of the substrate is thus in contact with the probe for 125 s. Considering the consistently lower contact pressures of the 10 μm/s experiment, poroelastic relaxation in both the probe and the substrate over that timespan likely led to the friction coefficient increase. Relaxation in the probe may be the key differentiator causing the drastic friction increase in the Gemini contact but not the migrating case.

With poroelastic relaxation occurring within the gradient layer, but no indication of dwell-induced friction, we must consider either how fluid squeeze-out is resisted, or how the water is retained. Similar Gemini experiments conducted at 6 kPa with 'brushy' 10% pAam by Simic et al. led them to conclude that rapid rehydration occurs during the period of time that the substrate is out of contact [18]. Their sliding speeds were as high as 15 mm/s across a 10 mm stroke length, implying that the rehydration process must take place within fractions of a second even at their large pressures and sliding speeds. Experiments by Gombert et al. with 'brushy' 7.5% pAam gels found friction to be speed-independent for speeds up to 10.5 mm/s [13]. They posit the presence of a resilient water layer held by the dangling chains at the less-crosslinked surface, and suggest that this rapidly rehydrating layer is primarily responsible for the tribological properties of the hydrogel.

In our sliding experiments, the stroke length was 1500 μm, while contact radii were at least 600 μm. A sliding speed of 100 μm/s would give the center of the substrate track 3 s to rehydrate in time for the next pass. This brief period of time out of contact appears sufficient to recapture the exuded water back into the 'brushy' layer, restoring its lubricity. The resulting non-transient friction behavior for the faster sliding speeds supports this notion of quick rehydration of the less-dense surface layer. Our present work confirms the presence of the less-dense, less-crosslinked surface layer of these hydrogels, and shows how their high lubricity is primarily a function of sliding speed.

While this current work thoroughly studies the effects of the surface gradient layer on its contact and sliding behavior, it does not directly image the polymer structure of the layer. Polymer density was determined in previous work by Gombert et al., confirming the less-dense nature of the polymer near the surface using neutron reflectometry and IR spectroscopy [13].

Transient behavior was seen for the slowest (10 μm/s) Gemini sliding experiment. This is most likely due to squeeze-out in the gel probe, which is under constant load throughout each test. Further investigation into the exact cause of the probe dehydration at slower speeds is needed.

The effect of compositional changes on the resulting contact behavior is also required. This would determine how the thickness of the non-Hertzian regime changes as the bulk gel structure changes. The thickness and relative gradient of

the polymer density at the surface likely affects the contact mechanics of the layer, as well as the friction seen during sliding.

Conclusion

Indentation, creep, and sliding experiments on migrating and Gemini contact setups of polyacrylamide gels confirmed the existence of a 'brushy' lower-density surface layer. This layer has a structure with gradient crosslink density that vanishes at the surface, which controlled the surface response of the hydrogels during indentation, creep, and sliding experiments.

Microscale indentation of these gels was not adequately predicted by Hertzian contact alone; contact areas were consistently underpredicted. Force-derivative analysis showed that the initial 13–29 μm of penetration is non-Hertzian, and that the thickness of the low-density gradient layer is likely around this magnitude. Creep experiments exhibited contact area growth as large as 40%. This relaxation is likely poroelastic in nature due to the agreeable diffusion constants obtained from poroelastic theory. Despite maximum pressures being only 10% of the osmotic pressure of these gels, the low-density surface layer allows local water squeeze-out within that layer. This is made possible from the larger effective pore sizes as the crosslink density decreases towards the surface. Friction during sliding was strongly dependent on the sliding speed, with slower sliding speeds experiencing higher friction. Contact area was not dependent on our tested sliding speeds. Transient frictional behavior was only observed at very slow speeds in Gemini contact, likely due to increased adhesion of the water-deficient probe to the substrate. This leads us to believe that rehydration of these hydrogels, and particularly the less-dense gradient layer, is a rapid process.

Knowledge of this less-dense gradient layer will be useful for designing hydrogels that require ultra-low friction and high lubricity with minimal changes to stiffness. Experimentation with other novel hydrogel systems, such as double networks, may allow more useful composite-structured gels to be created.

Acknowledgments This work was supported by the National Science Foundation through NSF Award 1751945. Thank you to Jiho Kim, Shabnam Bonyadi, Md Mahmudul Hasan, and Yaswanth Sai Jetti for helpful reviews and support.

Funding This work was supported by the National Science Foundation (Award 1751945).

Declarations

Conflict of Interest The authors declare that they have no conflict of interest.

References

1. DeRossi D, Kajiwara K, Osada Y, Yamauchi A (1991) Polymer Gels: Fundamentals and Biomedical Applications, vol. 53
2. Drury JL, Mooney DJ (2003) Hydrogels for tissue engineering: Scaffold design variables and applications. Biomaterials 24(24):4337–4351. https://doi.org/10.1016/S0142-9612(03)00340-5
3. Calvert P (2009) Hydrogels for soft machines. Adv Mater 21(7):743–756. https://doi.org/10.1002/adma.200800534
4. Haque MA, Kurokawa T, Gong JP (2012) Super tough double network hydrogels and their application as biomaterials. Polymer (Guildf) 53(9):1805–1822. https://doi.org/10.1016/j.polymer.2012.03.013
5. Gong JP, Katsuyama Y, Kurokawa T, Osada Y (2003) Double-network hydrogels with extremely high mechanical strength. Adv Mater 15(14):1155–1158. https://doi.org/10.1002/adma.200304907
6. Sun JY et al (2012) Highly stretchable and tough hydrogels. Nature 489(7414):133–136. https://doi.org/10.1038/nature11409
7. Lin P, Ma S, Wang X, Zhou F (2015) Molecularly engineered dual-crosslinked hydrogel with ultrahigh mechanical strength, toughness, and good self-recovery. Adv Mater 27(12):2054–2059. https://doi.org/10.1002/adma.201405022
8. Shoaib T, Espinosa-Marzal RM (2018) Insight into the Viscous and Adhesive Contributions to Hydrogel Friction. Tribol Lett 66(3):1–14. https://doi.org/10.1007/s11249-018-1045-7
9. Li H, Choi YS, Rutland MW, Atkin R (2020) Nanotribology of hydrogels with similar stiffness but different polymer and crosslinker concentrations. J Colloid Interface Sci 563:347–353. https://doi.org/10.1016/j.jcis.2019.12.045
10. Arjmandi M, Ramezani M, Nand A, Neitzert T (2018) Experimental study on friction and wear properties of interpenetrating polymer network alginate-polyacrylamide hydrogels for use in minimally-invasive joint implants. Wear 406–407(April):194–204. https://doi.org/10.1016/j.wear.2018.04.013
11. Shi Y, Xiong D (2013) Microstructure and friction properties of PVA/PVP hydrogels for articular cartilage repair as function of polymerization degree and polymer concentration. Wear 305(1–2):280–285. https://doi.org/10.1016/j.wear.2012.12.020
12. Meier YA, Zhang K, Spencer ND, Simic R (2019) Linking Friction and Surface Properties of Hydrogels Molded against Materials of Different Surface Energies. Langmuir 35(48):15805–15812. https://doi.org/10.1021/acs.langmuir.9b01636
13. Gombert Y, Simič R, Roncoroni F, Dübner, Geue T, Spencer ND (2019) "Structuring Hydrogel Surfaces for Tribology," Adv. Mater. Interfaces, vol. 6, no. 22, https://doi.org/10.1002/admi.201901320
14. Dunn AC, Urueña JM, Huo Y, Perry SS, Angelini TE, Sawyer WG (2013) Lubricity of surface hydrogel layers. Tribol Lett 49(2):371–378. https://doi.org/10.1007/s11249-012-0076-8
15. Garcia M, Schulze KD, O'Bryan CS, Bhattacharjee T, Sawyer WG, Angelini TE (2017) Eliminating the surface location from soft matter contact mechanics measurements. Tribol - Mater Surfaces Interfaces 11(4):187–192. https://doi.org/10.1080/17515831.2017.1397908
16. Chan EP, Hu Y, Johnson PM, Suo Z, Stafford CM (2012) Spherical indentation testing of poroelastic relaxations in thin hydrogel layers. Soft Matter 8(5):1492–1498. https://doi.org/10.1039/c1sm06514a
17. Lin DC, Shreiber DI, Dimitriadis EK, Horkay F (2009) Spherical indentation of soft matter beyond the Hertzian regime: Numerical and experimental validation of hyperelastic models. Biomech Model Mechanobiol 8(5):345–358. https://doi.org/10.1007/s10237-008-0139-9
18. Simic R, Yetkin M, Zhang K, Spencer ND "Importance of Hydration and Surface Structure for Soft-Hydrogel Friction."

19. Williams DRM (1993) Moduli of Polymer Brushes, Contact Mechanics, and Atomic Force Microscope Experiments. Macromolecules 26(19):5096–5098. https://doi.org/10.1021/ma00071a018
20. Rubinstein M, Colby RH (2003) Polymer Physics. Oxford University Press Inc, New York
21. Galli M, Comley KSC, Shean TAV, Oyen ML (2009) Viscoelastic and poroelastic mechanical characterization of hydrated gels. J Mater Res 24(3):973–979. https://doi.org/10.1557/jmr.2009.0129
22. Lin Y-Y, Hu B-W (2006) Load relaxation of a flat rigid circular indenter on a gel half space. J Non Cryst Solids 352(38):4034–4040. https://doi.org/10.1016/j.jnoncrysol.2006.07.007
23. Cuccia NL, Pothineni S, Wu B, Harper JM, Burton JC (2020) Pore-size dependence and slow relaxation of hydrogel friction on smooth surfaces. Proc Natl Acad Sci U S A 117(21):11247–11256. https://doi.org/10.1073/pnas.1922364117
24. Schulze KD et al (2017) Biotribology Polymer Osmotic Pressure in Hydrogel Contact Mechanics. Biotribology 11(May):3–7. https://doi.org/10.1016/j.biotri.2017.03.004
25. Kii A, Xu J, Gong JP, Osada Y, Zhang X (2001) Heterogeneous polymerization of hydrogels on hydrophobic substrate. J Phys Chem B 105(20):4565–4571. https://doi.org/10.1021/jp003242u
26. McGhee EO et al (2018) "In Situ Measurements of Contact Dynamics in Speed-dependent Hydrogel Friction," *Biotribology*, vol. 13, no. October 2017, pp. 23–29, https://doi.org/10.1016/j.biotri.2017.12.002
27. Kim J, Dunn AC (2016) Soft hydrated sliding interfaces as complex fluids. Soft Matter 12(31):6536–6546. https://doi.org/10.1039/c6sm00623j
28. Reale ER, Dunn AC (2017) Poroelasticity-driven lubrication in hydrogel interfaces. Soft Matter 13(2):428–435. https://doi.org/10.1039/C6SM02111E
29. Lai Y, He D, Hu Y (2019) Indentation adhesion of hydrogels over a wide range of length and time scales. Extrem Mech Lett 31:100540. https://doi.org/10.1016/j.eml.2019.100540